ChemCatChem

Research Article
doi.org/10.1002/cctc.202501334

Chemistry Europe
European Chemical Societies Publishing

www.chemcatchem.org

A Design of Experiment-Driven Optimization of NiMnAl Mixed Metal Oxide Catalysts for CO_2 Methanation

Dennis Weber,[a, b] Asad Asadli[+],[b] Adrian Seitz,[b] Andreas Hutzler,[c] Patrick Schühle,[b] and Tanja Franken*[a, b]

Power-to-gas technologies, including CO_2 methanation, offer a promising strategy for mitigating anthropogenic climate change. Nickel-based mixed metal oxide catalysts have demonstrated high activity, selectivity and stability in this challenging reaction in recent years. This study investigates the effects of synthesis parameters on the structure, activation, and reaction behavior of NiMnAl mixed metal oxide (MMO) catalysts. A Design of Experiment approach was employed to systematically vary the calcination temperature (500–950 °C), pH (8–10), and aging time (1–30 h) during synthesis by coprecipitation, resulting in the synthesis and testing of approximately 35 catalysts. The calcination temperature determines the catalyst structure, with metastable NiAl phases forming up to 650 °C and spinel phases forming above 800 °C. Notably, the spinel NiMnAl MMO catalysts exhibit superior performance, achieving approximately 60% higher methane formation rates per gram Ni of the catalyst compared to a supported industrial methanation reference catalyst (SPP2080-IMRC). Comprehensive characterization using XRD, elemental analysis, N_2 physisorption, TPR, CO_2-TPD, N_2O chemisorption, and STEM-EDXS provide insights into the catalysts' properties and activity.

1. Introduction

The mitigation of anthropogenic climate change, driven by the burning of fossil fuels and the subsequent emission of greenhouse gases, particularly CO_2, poses a significant challenge to today's society.[1,2] To address this challenge, developing technologies that utilize CO_2 as a resource is crucial for achieving net-zero emissions and creating a circular carbon economy. Carbon capture and utilization (CCU) strategies enable the conversion of CO_2 into valuable products, such as methanol, methane (Sabatier reaction Equation 1), and carbon monoxide (reverse water gas shift reaction (2)), among others.[3–5] The CO_2 required for these processes can be sourced from industrial waste gases, containing it in high concentrations, such as those emitted by cement production or waste incineration plants.[6] An important CCU strategy is CO_2 methanation, in which green hydrogen and captured CO_2 are catalytically converted into methane. Synthetic methane is an attractive energy carrier that can be integrated into existing fossil-fuel-related infrastructure and processes, as well as stored for later use:[4,7–9]

$$CO_2 + 4H_2 \rightleftharpoons CH_4 + 2H_2O, \quad \Delta_R H = -165.0\ \text{kJ mol}^{-1} \tag{1}$$

$$CO_2 + H_2 \rightleftharpoons CO + H_2O, \quad \Delta_R H = 42.1\ \text{kJ mol}^{-1} \tag{2}$$

$$CO + 3H_2 \rightleftharpoons CH_4 + H_2O, \Delta_R H = -206.3\ \text{kJ mol}^{-1} \tag{3}$$

The selectivity toward methane can be tuned by the catalyst choice and the process conditions. For nickel-based catalysts, the most relevant side reaction is the reverse water gas shift reaction (RWGS) (Equation 2), which becomes increasingly thermodynamically favorable at elevated temperatures. The CO produced in this reaction can subsequently undergo CO methanation (Equation 3), producing methane. Currently, supported Ni/Al_2O_3 is the state-of-the art catalyst for CO_2 methanation because of its high selectivity and cost efficiency. Nevertheless, the catalyst's activity and selectivity can decrease due to Ni sintering and the formation of the more stable $NiAl_2O_4$ spinel phase on the surface.[10–13] To address this issue, various promoters, including Mn and Fe, have been investigated to enhance the stability and productivity of the catalysts.[14–17]

In addition to supported catalysts, mixed metal oxide (MMO) catalysts are also used for CO_2 methanation due to their simple synthesis and considerable advantages in terms of activity and stability. Specifically, NiAl-based MMO catalysts are used,

[a] D. Weber, T. Franken
Technische Chemie 1, Technische Universität Darmstadt, Peter-Grünberg-Straße 8 64287, Darmstadt, Germany
E-mail: tanja.franken@tu-darmstadt.de

[b] D. Weber, A. Asadli[+], A. Seitz, P. Schühle, T. Franken
Institute of Chemical Reaction Engineering, Friedrich-Alexander-Universität Erlangen-Nürnberg, Egerlandstraße 3 91058, Erlangen, Germany

[c] A. Hutzler
Forschungszentrum Jülich GmbH, Helmholtz-Institute Erlangen-Nürnberg for Renewable Energy, Cauerstraße 1 91058, Erlangen, Germany

[+] Institute of Catalysis Research and Technology, Karlsruhe Institute of Technology, Hermann-von-Helmholtz-Platz 1, 76344, Eggenstein-Leopoldshafen, Germany

Supporting information for this article is available on the WWW under https://doi.org/10.1002/cctc.202501334

whereby the incorporation of Mn and Fe is being investigated as a means of increasing activity and stability. Recent studies on CO_2 methanation bulk MMO catalysts have primarily focused on hydrotalcite/layer double hydroxide (LDH)-derived catalysts, synthesized via coprecipitation and calcination at moderate temperatures (around 500 °C).[12,18–23] This approach has been widely adopted due to the ease of synthesis and the inherent advantages of hydrotalcite and LDH materials, including their high surface areas, tunable chemical compositions, and homogeneous distribution of active metal sites after calcination, which results in highly active catalysts.[12,18–24] However, higher calcination temperatures, which yield spinel MMO catalysts, have shown promising catalytic performances but have not yet been extensively researched.[25,26] This is mainly due to the challenges associated with activating the stable $NiAl_2O_4$ phase, which requires high reduction temperatures ($\geq$ 600 °C) and is therefore barely active in the methanation temperature range ($\leq$ 450 °C).[25,27] To overcome this limitation, we incorporated Mn into the spinel phase, which has been shown to significantly reduce the required reduction temperature to 450 °C, resulting in highly active and stable methanation catalysts (see Figures S1 and S2).[25]

This study aims to demonstrate the impact of varying synthesis parameters, including calcination temperature, pH, and aging time, on the structure, activation, and reaction behavior of NiMnAl MMO catalysts synthesized via coprecipitation. All NiMnAl MMO catalysts were synthesized with the same Mn/Ni target mass ratio of 0.39, which was selected based on its superior methanation performance demonstrated in our previous work.[25] The optimization of the synthesis parameters holds significant potential for enhancing catalytic performance, as previously demonstrated.[28–30] In addition, we enable a direct comparison between hydrotalcite/LDH-derived and spinel NiMnAl MMO catalysts, as well as with supported reference catalysts, providing valuable insights into the relationships between synthesis conditions, catalyst properties, and catalytic performance.

2. Results and Discussion

2.1. Characterization of Calcined NiMnAl Mixed Metal Oxide Catalysts and Reference Catalysts

The influence of the synthesis conditions on properties of NiMnAl-based mixed metal oxide (MMO) catalysts and their performance in CO_2 methanation was investigated in detail by varying pH from 8 to 10, aging time t_a from 1-30 h, and calcination temperature T_c from 500 to 950 °C during synthesis by coprecipitation.

The range of calcination temperatures and aging times was chosen based on the experimental conditions, feasibility, and prior publications.[12,25,26,31] The pH range was selected based on the Pourbaix diagrams of the metal ions and previous works.[12,21,25,26,31,32] To reach the optimal synthesis protocol, a Design of Experiment (DoE) approach with a face-centered central composite design illustrated in Figure 1 was used.

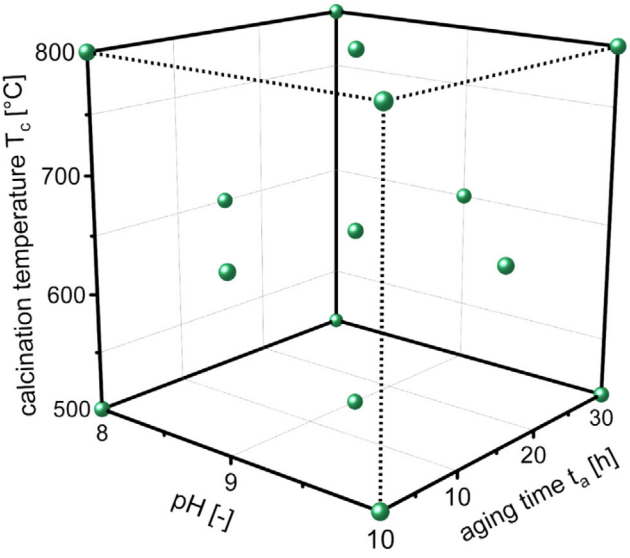

Figure 1. Design of Experiment plan to investigate the impact of synthesis parameters for the coprecipitation of NiMnAl mixed metal oxides with a face-centered central composite design.

For all catalysts a spinel composition of $Ni_{0.9}Mn_{0.375}Al_{1.625}O_4$ was targeted, which exhibits a Mn/Ni mass ratio of 0.39. This specific composition was chosen based on its superior catalytic performance described in our previous work (see Figure S1).[25] The modification with manganese was chosen for two key reasons: On the one hand previous studies have demonstrated that Mn incorporation can significantly enhance the CO_2 methanation performance, for example by providing basic MnO_x surface groups in spatial proximity to the Ni^0, which can enable alternative CO_2 activation pathways and thereby improve the performance of both mixed metal oxide and supported catalysts.[12,14,21,25,26,33] On the other hand, the incorporation of Mn into the spinel structure was found to induce lattice distortions, which can enhance the reducibility and facilitate the activation of the spinel phase under relevant activation conditions for the CO_2 methanation (Figure S2).[25,26,34]

The NiMnAl MMO catalysts synthesized by coprecipitation are designated NMAO-T_c-t_a-pH, where T_c stands for the calcination temperature, t_a indicates the aging time, and pH denotes the pH value of the precipitation medium. For example, NMAO-800C-1h-9 would refer to a catalyst that was calcined at 800 °C, aged for 1 h, and synthesized at a pH value of 9. For the discussion of the influence of calcination temperature, the designation for NiMnAl-MMO catalysts is simplified to NMAO-T_c (e.g., NMAO-800C) and implies a fixed set of synthesis conditions, namely a pH of 9 and an aging time of 15.5 h.

The subsequent discussion primarily focuses on the influence of calcination temperature, as it has the greatest impact on the resulting catalyst structure, properties, and performance. Nevertheless, the effects of pH and aging time and the comparison to the synthesis conditions used in a previous work (T_c = 800 °C, pH = 9, and t_a = 1 h),[25] as well as the comparison with reference catalysts, namely a self-synthesized supported NiO/Al_2O_3 catalyst and the Ni/Al_2O_3 SPP2080 industrial methanation reference catalyst (SPP2080-IMRC), are discussed.[33,35]

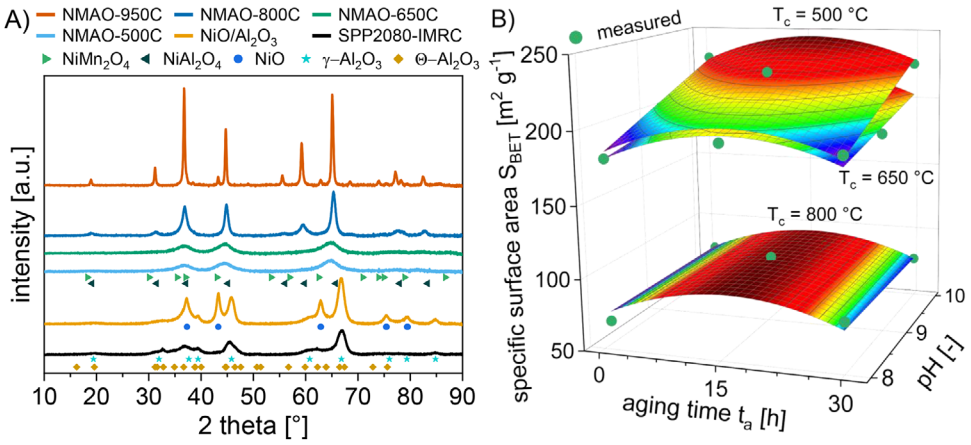

Figure 2. A) XRD patterns of NiMnAl mixed metal oxide calcined at 500, 650, 800, and 950 °C and supported reference catalysts as well as the following reference phases: $NiMn_2O_4$ (ICSD: 98-024-6769), $NiAl_2O_4$ (ICSD: 98-024-7086), NiO (ICSD: 98-008-7108), γ-Al_2O_3 (ICSD: 98-009-9836), and Θ-Al_2O_3 (ICSD: 98-008-2504). B) Design of Experiment results for specific surface area and measured data points, obtained through linear regression analysis, based on the data in Table S1 and the model shown in Table S2.

Table 1. Elemental composition measured by inductively coupled plasma atomic emission spectroscopy (ICP AES) and specific surface area and pore volume measured by N_2 physisorption of the different catalysts.

Sample /synthesis conditions	Elemental analysis Ni (wt.%)	Mn (wt.%)	Al (wt.%)	Mn/Ni ratio	Specific surface area S_{BET} (m^2 g^{-1})	Pore volume (cm^3 g^{-1})
NMAO-500C T_c = 500 °C, pH = 9, t_a = 15.5 h	27.2	8.7	21.8	0.320	229	0.75
NMAO-650C T_c = 650 °C, pH = 9, t_a = 15.5 h	27.7	9.7	22.4	0.349	212	0.65
NMAO-800C T_c = 800 °C, pH = 9, t_a = 15.5 h	24.8	8.4	19.5	0.340	97	0.40
NMAO-950C T_c = 950 °C, pH = 9, t_a = 15.5 h	22.5	8.5	18.7	0.379	16	0.22
NMAO-800C-1h-9 T_c = 800 °C, pH = 9, t_a = 1	28.3	9.8	23.5	0.346	94	0.40
15 wt.% NiO/Al_2O_3	14.4	–	–	–	100	0.71
SPP2080-IMRC (Ni/Al_2O_3)[35]	8.6	–	–	–	144	0.4

The Ni/Al_2O_3 (SPP2080-IMRC) reference catalyst properties are discussed in detail elsewhere,[33,35] but the key properties are added to facilitate comparability. The X-ray diffraction (XRD) patterns show that the self-synthesized supported NiO/Al_2O_3 catalyst contain NiO and γ-Al_2O_3 phases, whereas the SPP2080-IMRC shows mainly γ- and Θ-Al_2O_3, with NiO barely visible, consistent with previous findings (Figure 2).[35] The XRD patterns of the coprecipitated NiMnAl mixed metal oxide catalysts which were synthesized with a calcination temperature of 500 °C and 650 °C exhibit three broad reflexes approximately matching the main features of the $NiAl_2O_4$ spinel phase (see Figures 2A and S3). These features were described earlier for similar synthesis conditions and assigned to metastable NiAl mixed metal oxide phases, while the addition of Mn seemed to not significantly impact the resulting XRD patterns, as shown by Burger et al.[12] For a calcination temperature of 800 °C, the XRD pattern corresponds to a single spinel phase, which can be identified by comparison with reference patterns to a phase with a spinel structure (space group Fd3m). A slight left shift compared to the reflex positions of $NiAl_2O_4$ confirms the incorporation of Mn into the nickel aluminate spinel phase, as shown previously.[25] A calcination temperature of 950 °C leads to an increase in crystallinity and a segregation of a separate NiO phase.

The specific surface area and pore volume of the catalysts are halved at calcination temperatures above 800 °C and continue to decrease rapidly at higher temperatures (see Figure 2B, Tables 1 and S1). This could be due to further sintering of the pore structure of the NiMnAl mixed metal oxides as the calcination temperature increases. In addition, the pH value has a significant influence on the pore volume, with a rapid increase observed at pH values above 8, while the aging time has no significant influence on either the specific surface area or the pore volume. (cf. Figure S4A, Tables 1 and S1).

Inductively coupled plasma atomic emission spectroscopy (ICP AES) was used to determine the Mn/Ni mass ratios (see Tables 1 and S1). The Mn/Ni ratio increases significantly with

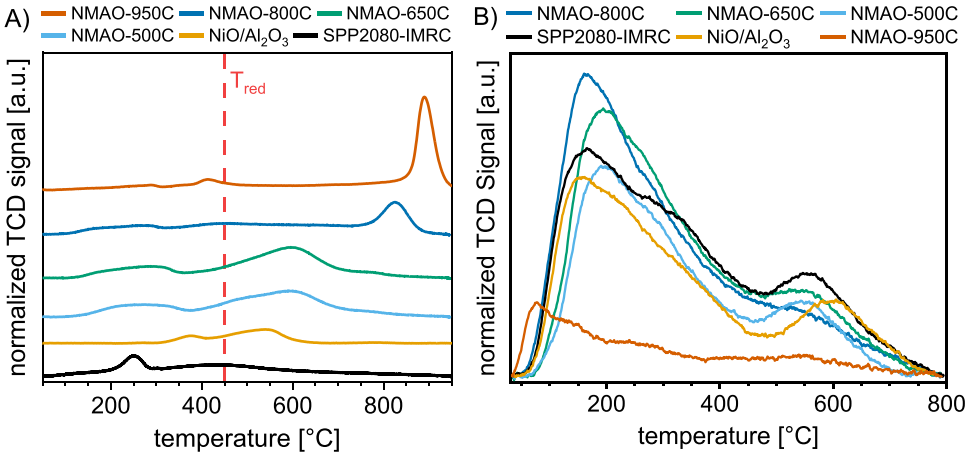

Figure 3. A) TPR profiles of NiMnAl mixed metal oxide calcined at 500, 650, 800, and 950 °C and supported reference catalysts. Conditions: 10% H_2 in Ar with a flow rate of 50 mL min^{-1}, *R*amp: 5 K/min. B) CO_2-TPD profiles of NiMnAl MMO and supported reference catalysts. Conditions: *R*amp: 5 K min^{-1} in He, pretreatment: 10% H_2 in Ar with a flow rate of 50 mL min^{-1} at 450 °C for 1 h, adsorption: pure CO_2 with a flow rate of 20 mL min^{-1} at 100 °C for 1 h.

Table 2. Characterization and performance of the catalyst: H_2 uptake of calcined catalysts (TPR according to activation conditions, see Figure S7) and properties of the reduced catalyst, including active Ni surface area (N_2O titration), CO_2 adsorption capacity (CO_2-TPD, weak and medium basic sites, see Figure S8), methane formation rates, and methane formation rates per g_{Ni} measured at 350 °C after reduction according to the experimental pretreatment conditions.

Sample	H_2 uptake upon reduction (mmol g_{cat}^{-1})	Weak and medium basic sites (mmol g_{cat}^{-1})	Normalized active Ni surface area $A_{Ni,norm}$ (m^2 g_{cat}^{-1})	Methane formation rate r_{CH_4} (mol(CH_4) h^{-1} g_{cat}^{-1})	Methane formation rate per $g_{Ni,cat}$ $r_{CH_4,Ni}$ (mol(CH_4) h^{-1} $g_{Ni,cat}^{-1}$)
NMAO-500C	1.4	0.35	0.1	0.49	1.8
NMAO-650C	1.4	0.42	0.4	0.77	2.8
NMAO-800C	1.6	0.50	4.9	1.03	3.8
NMAO-950C	0.9	0.09	0.1	0.16	0.7
NMAO-800C-1h-9	1.6	0.52	4.2	0.82	2.9
15 wt.% NiO/Al_2O_3	0.7	0.37	1.6	0.15	1.0
SPP2080-IMRC	0.6	0.45	0.7	0.21	2.4

increasing pH and approaches the target ratio of 0.39 at a pH of 10 (Table S1). In contrast, no systematic correlation between the calcination temperature or aging time and the Mn/Ni ratio is evident (Figures S4B and S1). The large difference in the Mn/Ni ratio at pH 8 ($\leq$0.29) can be explained by incomplete precipitation of Mn, which is consistent with the prediction of the combined Ni, Mn, and Al Pourbaix diagram (Figure S5).

2.2. Activation of NiMnAl Mixed Metal Oxide Catalysts by Reduction

The reductive activation behavior of NiMnAl-MMO catalysts was analyzed using a combination of temperature-programmed reduction (TPR), X-ray diffraction (XRD), and high-angle annular dark field scanning transmission electron microscopy (HAADF-STEM) in conjunction with energy-dispersive X-ray spectroscopy (EDXS). The TPR measurements show at least one reduction peak below and above the reduction temperature of 450 °C used in the methanation experiments for all catalysts (cf. Figures 3A and S6). As described in the literature, the low and high temperature peaks can be assigned to differently sized or bound NiO particles on the Al_2O_3 surface.[35,36]

As the calcination temperature of the NiMnAl MMO catalysts increases from 500–950 °C, the high-temperature reduction peak shifts to higher temperatures, while the position of the low-temperature peak is barely changed (Figure 3). The shift in the high-temperature peak is most likely due to the formation of the NiMnAl spinel phase at a calcination temperature of 800 °C or higher. The spinel phase is very stable and therefore difficult to reduce.[25,27,36] The low temperature peak of the NiMnAl MMO catalysts can be attributed to the reduction of Mn^{3+} to Mn^{2+} as described previously,[12,33,37] whereas the high temperature peak is most likely associated with the reduction of Ni^{2+} to Ni^0.[12,36]

The CO_2 adsorption capacity, as determined by temperature-programmed desorption of CO_2 (CO_2-TPD), exhibits a notable increase in the amount of weak and medium basic sites up to a calcination temperature of 800 °C, which are crucial for the methanation performance (Figure 3B and Tables 2 and S3).[12,14,38] At a calcination temperature of 950 °C, H_2 consumption and CO_2 capacity decrease rapidly (see Table 2). In addition, only the

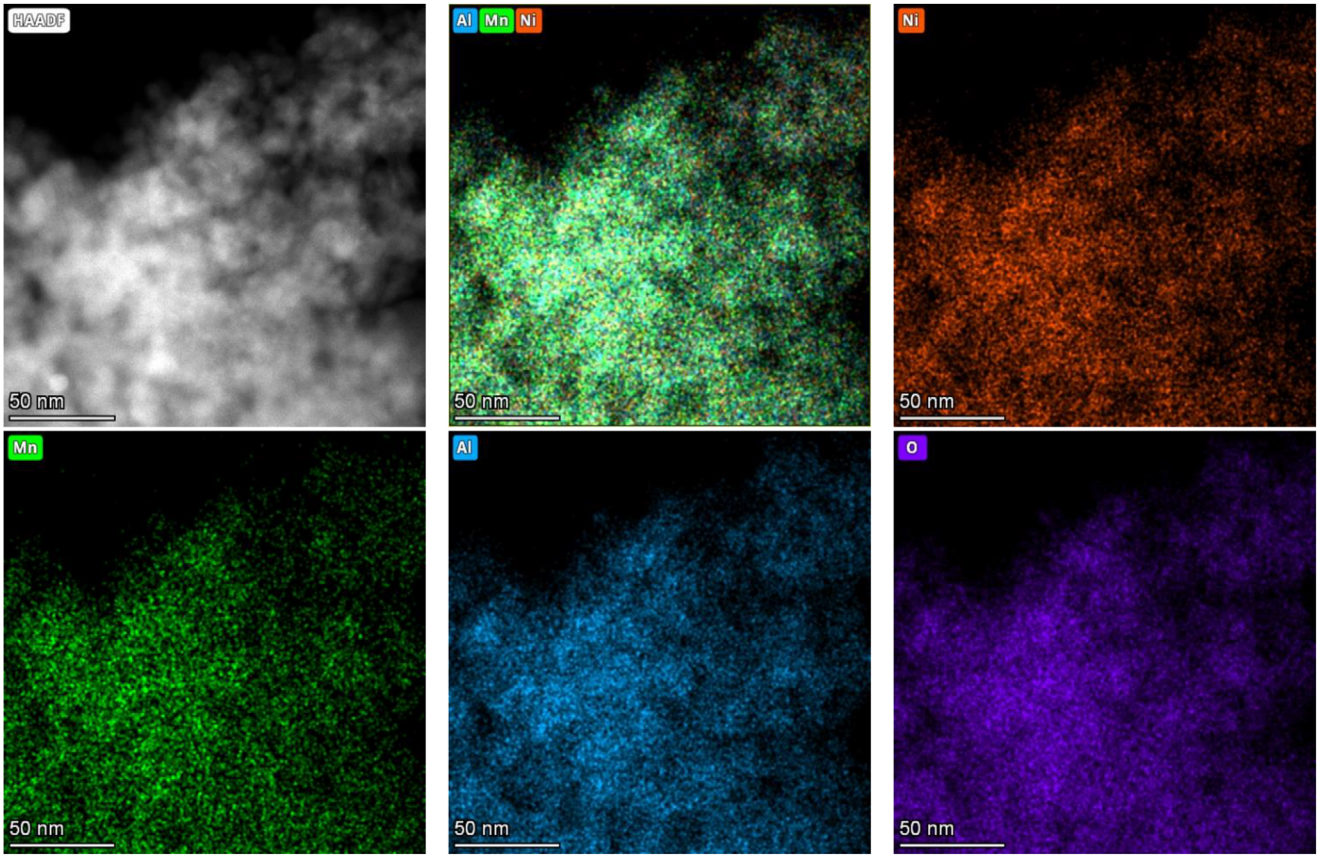

Figure 4. HAADF-STEM and STEM-EDXS imaging of reduced NMAO-800C-1h-9 catalyst, reduction conditions: 5% H_2 in N_2 at 450 °C for 1 h.

NiMnAl spinel catalysts calcined at 800 °C show a significantly higher active nickel surface area, measured by N_2O titration, than the supported reference catalysts, while all other calcination temperatures exhibit lower $A_{Ni'}$ (Table 2).

Ex situ STEM-EDXS and XRD analysis was performed to investigate the reductive activation behavior of NiMnAl spinel MMO (NMAO-800C-1h-9) at different reduction temperatures. The STEM-EDXS images shown in Figure 4 depict a homogeneous distribution of Ni throughout the whole sample after a reduction at 450 °C, with no discernible differences between the calcined and reduced catalysts (cf. Figures 4 and S9). The absence of visible Ni nanoparticles of the reduced catalysts emphasizes the high Ni dispersion. Furthermore, the NiMnAl spinel catalyst exhibits a very high active Ni surface area of 4.9 $m^2\ g_{cat}^{-1}$, as measured by N_2O titration, indicating the activation of the catalyst's surface leading to very small Ni nanoparticles. Increasing the reduction temperature to 600 °C leads to the formation of visible Ni nanoparticles on the surface of the NiMnAl spinel phase, while the underlying MMO structure remains intact (Figure 5). This indicates that the activation of the NiMnAl spinel catalyst calcined at 800 °C occurs most likely through the exsolution of Ni, which is consistent with previous reports on similar systems.[27,39]

Further analysis of the reduced NiMnAl spinel catalyst by XRD provides additional evidence, revealing the presence of Ni^0, which can only be identified after reduction at 600 °C using the non-overlapping reflection at $2\Theta = 51.7°$ (red box) in Figure 6. In contrast, no clear Ni^0 reflections can be observed at 450 °C (Figure 6). Moreover, the Ni crystallite size, calculated using the Scherrer equation, is found to be smaller for the 600 °C reduced NiMnAl spinel catalyst compared to the 450 °C reduced supported NiO/Al_2O_3 reference catalyst (cf. Figure 6 and Table S4). This is also evident in the STEM-EDXS images, which show broader NiO and Ni nanoparticle distribution of the calcined and reduced supported NiO/Al_2O_3 reference catalyst (see Figures S10 and S11).

2.3. Reaction Behavior of NiMnAl Mixed Metal Oxide Catalysts

All experiments were carried out in a fixed-bed reactor operated at temperatures ranging from 250 to 450 °C and at ambient pressure. The Design of Experiment (DOE) plan (Figure 1), which involved the synthesis of two batches for each catalyst, resulted in the synthesis and testing of about 35 catalysts. A high space velocity (SV) of 26.2 mL min^{-1} mg_{cat}^{-1} was employed in the fixed bed reactor to evaluate reaction rates, avoid thermodynamic equilibrium, and assess catalyst stability.

The NMAO-800C-30h-10 catalyst and the reference catalysts showed negligible deactivation in 40-h stability tests (see Figure S12). Furthermore, the reproducibility of the coprecipitation method for synthesizing NiMnAl-MMO catalysts was confirmed by the comparable methanation performance of duplicate synthesis batches (Figure S13).

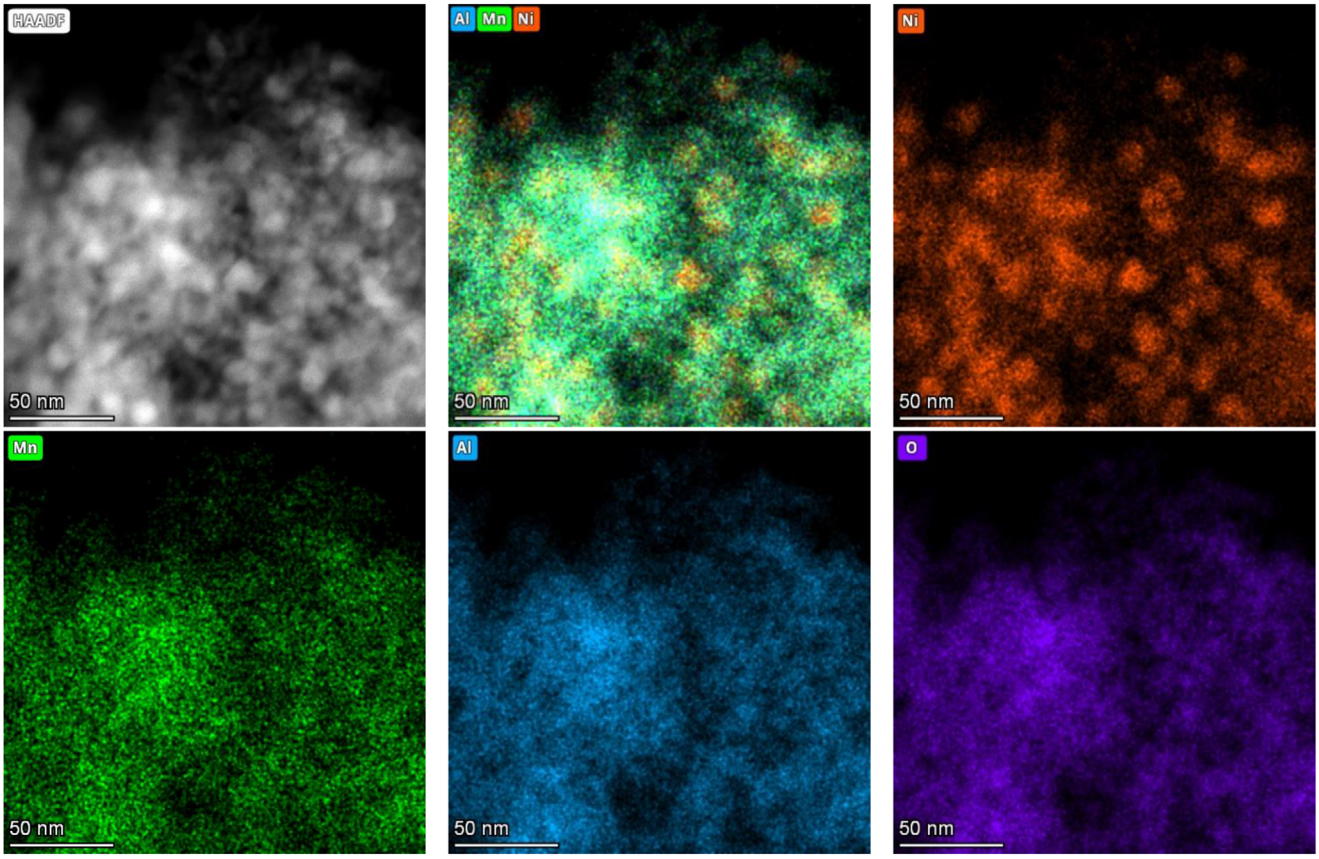

Figure 5. HAADF-STEM and STEM-EDXS spectrum imaging of reduced NMAO-800C-1h-9 catalyst, reduction conditions: 5% H_2 in N_2 at 600 °C for 1 h.

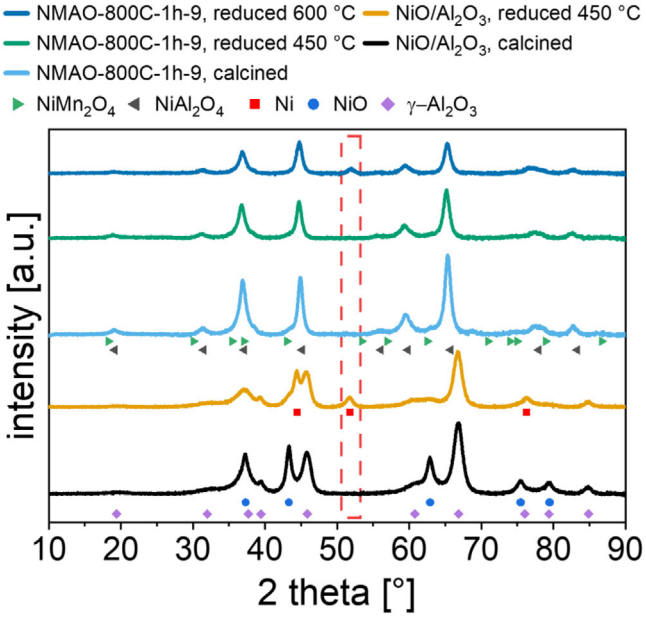

Figure 6. Ex situ XRD patterns of calcined and reduced NiMnAl spinel and supported NiO/Al_2O_3 catalyst, as well as the following reference phases: $NiMn_2O_4$ (ICSD: 98-024-6769), $NiAl_2O_4$ (ICSD: 98-024-7086), Ni^0 (ICSD: 98 007 6667), NiO (ICSD: 98-008-7108) and γ-Al_2O_3 (ICSD: 98-009-9836), red box: non-overlapping reflex of Ni^0, reduction conditions: 5% H_2 in N_2 at 450 °C/600 °C for 1 h.

During the activation of the supported catalysts surface NiO reduces to Ni^0 which can facilitate CO_2 and H_2 activation. Therefore, the NiO crystallite size and distribution has an impact on the Ni nanoparticle size and can lead to the differences in catalytic performance of the shown supported catalysts, despite the higher Ni loading and active Ni surface area (A_{Ni}) of the self-synthesized NiO/Al_2O_3 catalyst (cf. Table 2 and Figure 7). The selectivity of the supported reference catalyst exhibits an S-shaped trend, consistent with literature reports for similar systems.[35] This behavior can be attributed to the temperature-dependent interplay between the reverse water-gas shift (RWGS), CO_2 methanation, and CO methanation reactions.[40,41]

In contrast, the NiMnAl MMO catalyst displays a less pronounced S-shaped trend, potentially due to the presence of basic MnO_x and AlO_x surface groups in the MMO phase, which provide alternative CO_2 activation pathways.[26,33] The calcination temperature has a significant influence on the catalytic performance of NiMnAl-MMO catalysts, with a significant increase in CO_2 conversion and CH_4 selectivity observed up to a calcination temperature of 800 °C, but performance rapidly decreases above this temperature. (Figure 7)

A comparison of catalysts calcined at 500 and 650 °C reveals negligible differences in crystal structure, specific surface area, pore volume, and H_2 consumption (see cf. Figure 2A and Tables 1 & 2). However, the increase in CO_2 adsorption capacity and active Ni surface area after activation results in a 60% increase in

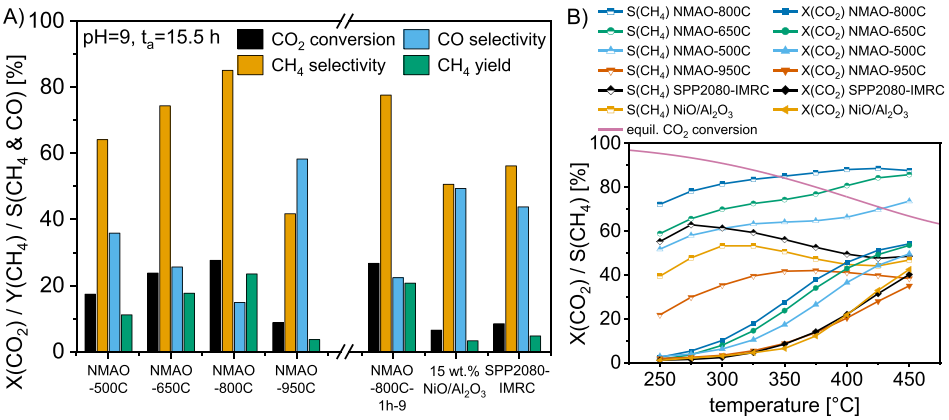

Figure 7. A, B) Catalytic performance comparison of NiMnAl mixed metal oxide calcined at 500, 650, 800, and 950 °C, and supported reference catalysts in the methanation of CO_2. Conditions: pretreatment—10% H_2 in Ar at 450 °C for 1 h, methanation—c(CO_2) = 6.25 vol%, CO_2/H_2 = 1/4 diluted in Ar, m(cat) = 20 mg diluted in 2.5 g quartz sand, total flow rate—523.6 mL min^{-1}, GHSV = 20,000 h^{-1}, SV = 26.18 mL min^{-1} mg_{cat}^{-1}, p = 1 bar.

methane formation rate (see Figure 7 and Tables 1 & 2). Further increasing the calcination temperature to 800 °C leads to a significant increase in H_2 consumption, CO_2 adsorption capacity, and Ni surface area, resulting in a further 40% increase in methanation formation rate. The optimal calcination temperature of 800 °C leads to a doubling of the methane formation rate compared to 500 °C, which is due to several reasons. On the one hand, the calcination temperature of 800 °C leads to a significant increase in the number of weak and medium basic sites as well as to a change in activation behavior, which ultimately results in a significantly higher active Ni surface area. On the other hand, the spatial proximity between the basic groups and the exsolved Ni^0 within the spinel phase may play a crucial role in improving the methanation performance of the catalyst. In contrast, a calcination temperature above 800 °C leads to a rapid decline in H_2 consumption, CO_2 adsorption capacity, and active Ni surface area, resulting in a low methanation rate, in a similar range to that of a self-synthesized supported NiO/Al_2O_3 catalyst (cf. Figure 7 and Tables 1 & 2).

For further comparison, we added a comprehensive comparison with different mixed metal oxide and supported catalysts presented in the literature (see Table S5). The NMAO-800C spinel catalyst has the highest methane formation rate of all the referenced catalysts and, despite its relatively high nickel content, also achieves one of the highest methane formation rates per gram nickel of the catalyst ($g_{Ni,cat}$).

The resulting model (see Figure 8 and Table S6) describes the experimental data reasonably well and illustrates the previously discussed performance trends. The pH value and aging time during catalyst synthesis are also crucial factors that influence catalytic performance. It is noteworthy that when comparing the optimized synthesis (NMAO-800C-30h-10) with the synthesis conditions (T_c = 800 °C, pH = 9, and t_a = 1 h) from our previous study (cf. Table 2 and Figures 7 and S14), a 25% increase in the methane formation rate is observed.[25] This is also evident from the fact that a pH value of 8 leads to a lower Mn/Ni mass ratio and poorer methanation performance Figure 8. However, it should be noted that variations in the Mn/Ni mass ratio, as observed here, do not have a significant impact on

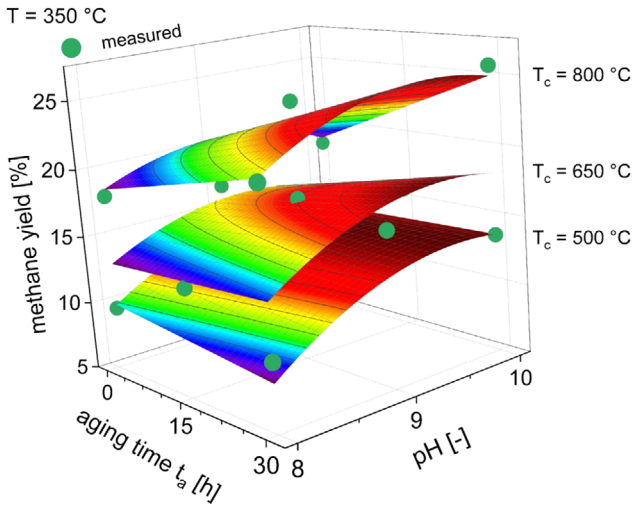

Figure 8. Design of Experiment results for the methane yield and measured data points, obtained through linear regression analysis, based on the experimental data depicted in Figure S14 and the model shown in Table S6. Conditions: pretreatment—10% H_2 in Ar at 450 °C for 1 h, methanation—c(CO_2 = 6.25 vol%, CO_2/H_2 = 1/4 diluted in Ar, m(cat) = 20 mg diluted in 2.5 g quartz sand, total flow rate—523.6 mL min^{-1}, GHSV = 20,000 h^{-1}, SV = 26.18 mL min^{-1} mg_{cat}^{-1}, p = 1 bar.

the catalytic properties and performance, as demonstrated by the comparable methanation performance of a spinel catalyst with an Mn/Ni ratio of 0.23 ($Ni_{0.9}Mn_{0.25}Al_{1.75}O_4$, see Figure S1).[25] The reduced methanation performance may be attributed to the decreased pore volume and specific surface area, which could potentially impact the activation behavior and active Ni surface area. In general, a higher pH and aging times tend to be beneficial, although the differences between 15.5 h and 30 h of aging time and pH 9 and 10 are relatively small (cf. Figures 8 and S14).

Therefore, it is unlikely that further increasing the pH and aging time would yield significant benefits. Moreover, higher pH values require more thorough washing after coprecipitation to prevent the formation of secondary phases. Inadequate washing of the catalysts can lead to the formation of NiO as a secondary phase, which can significantly reduce the performance of the

spinel phase (see Figure S15 and Table S4). The presence of NiO is presumably responsible for the reduced methane selectivity, comparable to that of the self-synthesized NiO/Al_2O_3 reference catalysts, as it may alter the activation and reaction behavior of the catalyst. Specifically, the presence of NiO could potentially block basic MnO_x and AlO_x surface groups of the spinel phase, thereby hindering alternative CO_2 activation pathways (Table S4).[26,33] Furthermore, the spatial proximity between these basic groups and the exsolved Ni^0 within the spinel phase may play a crucial role in the catalyst's methanation performance. This might also be one of the reasons that NMAO-950C performs so poorly, as it also contains NiO as a secondary phase Figure 2A.

3. Conclusion

This study employs a Design of Experiment (DOE) approach to investigate the impact of synthesis parameters, including calcination temperature, aging time, and pH, on the structure, activation, and reaction behavior of NiMnAl mixed metal oxide (MMO) catalysts for CO_2 methanation. The DOE plan with duplicate syntheses for each catalyst resulted in the synthesis and testing of about 35 catalysts. Through the application of DOE methodology, we have successfully optimized the synthesis parameters for the NiMnAl MMO catalysts, identifying the ideal conditions as a calcination temperature of 800 °C, a pH of 10, and an aging time of 30 h.

The calcination temperature determines the catalyst structure, with metastable NiAl oxide phases forming at temperatures up to 650 °C and spinel phases forming at temperatures above 800 °C. This structural change has a profound impact on the catalytic performance, with an optimal calcination temperature of 800 °C resulting in a doubling of the methane formation rate compared to calcination of the same catalyst composition at 500 °C. The NiMnAl spinel catalysts exhibit superior performance, achieving approximately 60% higher methane formation rates per gram Ni of the catalyst compared to a supported industrial methanation reference catalyst (SPP2080-IMRC). This enhanced performance can be attributed to the increase in the number of weak and medium basic sites, as well as the change in activation behavior of the NiMnAl spinel catalyst via Ni exsolution, leading to a very high active Ni surface area. Furthermore, spatial proximity between the basic groups and the exsolved Ni^0 within the spinel phase may play a crucial role in improving the methanation performance of the catalyst.

Moreover, higher pH values and longer aging times tend to be beneficial for the catalytic performance, as evidenced by a 25% increase in methane formation rate when comparing the catalyst from the optimized synthesis (NMAO-800C-30h-10) to the synthesis conditions (T_c = 800 °C, pH = 9, and t_a = 1 h) from a previous study.[25] However, it is crucial to carefully control the synthesis conditions to avoid secondary phases such as NiO, particularly for the NiMnAl spinel catalysts, as these can lead to a significant decrease in methanation performance. In summary, this study elucidates the importance of the right synthesis conditions for mixed metal oxide catalysts. It shows the complex interplay between synthesis parameters, catalyst structure, and reaction behavior, contributing to the development of highly efficient and stable catalysts for CO_2 methanation. Furthermore, this study demonstrates the strength of the DOE catalyst optimization approach, revealing the impacts of the reaction conditions on the reactivity with a reasonable number of catalyst syntheses to find the global optimal synthesis conditions.

4. Experimental Section

4.1. Catalyst Preparation

$Ni_{0.9}Mn_{0.375}Al_{1.625}O_4$ catalysts were prepared by coprecipitation of the corresponding nitrates with one molar sodium hydroxide. For this purpose, $Ni(NO_3)_2 \bullet 6\ H_2O$ (VWR Chemicals, 99.2%), $Mn(NO_3)_2 \bullet 4\ H_2O$ (Alfa Aesar, 98%) and $Al(NO_3)_3 \bullet 9\ H_2O$ (VWR Chemicals, 98.5%) were dissolved in deionized water. The pH was kept constant at a value between 8 and 10 by simultaneously adding the nitrates and NaOH using a Metrohm Eco Titrator and Dosimator. The solution was then aged with stirring for 1–30 h, the precipitate filtered off, and the catalyst was washed to neutrality with deionized water. The catalyst was dried overnight at 75 °C and calcined in air at 500–950 °C for 6 h with a heating ramp of 5 K/min. A NiO/Al_2O_3 catalyst was prepared by incipient wetness impregnation of $Ni(NO_3)_2 \bullet 6\ H_2O$ with the Al_2O_3 support (Puralox TH 100/150 from Sasol). The catalyst was dried overnight at 75 °C and calcined in air at 500 °C for 6 h with a heating ramp of 5 K min^{-1}.

4.2. Catalyst Characterization

4.2.1. X-ray Powder Diffraction

X-ray powder diffraction of the catalysts was studied using a Philips X'Perts X-ray diffractometer using Cu Kα radiation at an angle of 10° to 90° with a step size of 0.017° and 100 s per step.

4.2.2. N_2 Physisorption

The specific surface areas (S_{BET}) and pore volume were determined by N_2 physisorption in a Quantachrome QuadraSorb SI using the Quadrawin software. The total pore volume was determined at $p/p_0 \geq 0.99$, and the specific surface area was determined with the Brunauer–Emmett–Teller method at $p/p_0 = 0.05–0.21$. Prior to sorption measurements, the samples were degassed at 200 °C for 12 h in vacuum.

4.2.3. Inductively Coupled Plasma Atomic Emission Spectroscopy (ICP-AES)

The composition of the synthesized catalysts was determined by elemental analysis using inductively coupled plasma atomic emission spectroscopy (ICP-AES) with a SPECTRO Ciros CCD.

4.2.4. Temperature Programmed Reduction

The AutoChem II & HP from Micromeritics was used for temperature-programmed reduction. After purging in Ar at 450 °C for 0.5 h and cooling, the samples were heated to 950 °C with a ramp of 5 K min^{-1} in 10% H_2 in Ar. All steps were carried out at a flow rate of 50 mL

min^{-1}. The H_2 uptake was measured according to the activation conditions of the CO_2 methanation tests (10% H_2 in Ar at 450 °C for 1 h) and then calculated by integrating the resulting TCD signal versus time diagrams (see Figure S7).

4.2.5. Temperature Programmed Desorption

Temperature programmed desorption of CO_2 was conducted using an AutoChem II & HP from Micromeritics. Prior to analysis, pretreatment was carried out in 10% H_2 in Ar with a flow rate of 50 mL min^{-1} at 450 °C for 1 h. All subsequent steps were carried out at a flow rate of 20 mL min^{-1}. After purging for 0.5 h and cooling down in He, pure CO_2 was adsorbed at 100 °C for 1 h, followed by a 1 h purge with He. CO_2-TPD was carried out in He with a ramp of 5 K min^{-1} up to 800 °C. The amount of weak, medium, and strong basic sites is calculated by deconvolution and integration of the CO_2-TPD measurements (TCD signal versus time diagrams, see Figure S8).

4.2.6. High-Angle Annular Dark Field Scanning Transmission Electron Microscopy (HAADF-STEM) and Energy-Dispersive X-ray Spectroscopy (EDXS)

High-angle annular dark field scanning transmission electron microscopy (HAADF-STEM) was used for the estimation of the metal distribution and the nanoparticle size of the reduced catalysts, in conjunction with energy-dispersive X-ray spectroscopy (EDXS). The work was carried out using a Talos F200i (ThermoFisher Scientific) with an acceleration voltage of 200 kV. Remote air plasma cleaning was performed using a Tergeo-EM plasma cleaner (PIE Scientific) to remove adsorbed hydrocarbons and thus reduce carbon deposition during imaging.

4.2.7. N_2O Titration

The AutoChem II & HP from Micromeritics was used for N_2O titration. Pretreatment was carried out in 10% H_2 in Ar with a flow rate of 50 mL min^{-1} at 450 °C for 1 h, which corresponds to the pretreatment conditions in the catalytic experiments. The sample is then purged at 500 °C for 0.5 h in He. N_2O titration is performed by passing 40 mL min^{-1} 0.5% N_2O in He over the sample and measuring the resulting nitrogen according to reaction 4 with a thermal conductivity detector. The excess N_2O is removed in a cold trap with liquid nitrogen. The active nickel surface area is estimated according to Tada et. al. using Equation (5),[42] where n_{N2} is the amount of N_2 produced (mol), N_A is the Avogadro constant, S_{Ni} is the number of Ni surface atoms per unit area ($1.54 \bullet 10^{19}$ m^{-2}), and m_{cat} is the amount of catalyst used:[42]

$$Ni + N_2O \rightarrow NiO + N_2 \tag{4}$$

$$A_{Ni} = \frac{n_{N2} \cdot N_A}{S_{Ni}} \tag{5}$$

$$A_{Ni,norm} = \frac{A_{Ni}}{m_{cat}} \tag{6}$$

4.3. Catalytic Testing

4.3.1. CO_2 Methanation Experiments

Catalytic experiments were performed in a fixed-bed reactor with a diameter of 10 mm at ambient pressure. For each experiment, 0.02 g of 100–150 µm catalyst was used and diluted in 2.5 g of 200–300 µm quartz sand. Pretreatment was carried out at 450 °C in 10% H_2 in Ar for 1 h, followed by a run-in period of 6 h at 450 °C under methanation conditions. The CO_2 methanation was performed with a H_2/CO_2 ratio of 4/1 diluted in 68.75% Ar, a total flow rate of 523.6 mL min^{-1}, resulting in a gas hourly space velocity (GHSV) of 20,000 h^{-1}. The temperature was changed from 250 to 450 °C in 25 K increments. The gas flow was controlled with mass flow controllers (Bronkhorst EL-Flow), and the relative concentrations of the product gases were analyzed with a Pfeiffer Vacuum OmniStar GSD 350 mass spectrometer. The only byproduct detected was CO. Therefore, the CO_2 conversion (Equation 7), CH_4 selectivity (Equation 8), and CH_4 yield (Equation 9) were calculated using the following equations. The methane formation rates are calculated using Equations (10) and (11), where the amount of methane produced per gram of catalyst (Equation 10) and per gram of nickel in the catalyst (Equation 11), respectively, are determined based on the inlet CO_2 volume flow ($\dot{V}_{CO_2,in}$) and the resulting CH_4 yield, under the assumption of ideal gas behavior.

$$X(CO_2) = \frac{(n_{CO_2\,in} - n_{CO_2\,out})}{n_{CO_2\,in}} \times 100\% \tag{7}$$

$$S(CH_4) = \frac{(n_{CH_4\,out} - n_{CH_4\,in})}{(n_{CH_4\,out} - n_{CH_4\,in}) + (n_{CO\,out} - n_{CO_{in}})} \times 100\% \tag{8}$$

$$Y(CH_4) = X(CO_2) \cdot S(CH_4) \tag{9}$$

$$r_{CH_4} = \frac{\dot{V}_{CO_2,in} \cdot Y(CH_4) \cdot p_N}{R \cdot T_N \cdot m_{cat}} \tag{10}$$

$$r_{CH_4,Ni} = \frac{\dot{V}_{CO_2,in} \cdot Y(CH_4) \cdot p_N}{R \cdot T_N \cdot m_{Ni,cat}} \tag{11}$$

Acknowledgments

The authors kindly acknowledge funding by the German Research Foundation (DFG, FR 3856/2-2) in the framework of the priority program SPP2080 "DynaKat - Catalysts and reactors under dynamic conditions for energy storage and conversion". T.F. additionally acknowledges the funding by the SPP2080 "DynaKat" Early Career Research Scholarship for female scientists and by the Cluster of Excellence Engineering of Advanced Materials through the EAM Starting Grant.

Open access funding enabled and organized by Projekt DEAL.

Conflict of Interests

The authors declare no conflict of interest.

Data Availability Statement

The data that support the findings of this study are openly available in [Zenodo] at [https://doi.org/10.5281/zenodo.16993890], reference number [1].

Keywords: CO_2 methanation · Design of Experiment · Mixed metal oxides · Ni catalyst

[1] S. V. Krupa, R. N. Kickert, *Environ. Pollut.* **1989**, *61*, 263–393.
[2] M. Meinshausen, S. J. Smith, K. Calvin, J. S. Daniel, M. L. T. Kainuma, J.-F. Lamarque, K. Matsumoto, S. A. Montzka, S. C. B. Raper, K. Riahi, A. Thomson, G. J. M. Velders, D. P. P. van Vuuren, *Clim. Change* **2011**, *109*, 213–241, https://doi.org/10.1007/s10584-011-0156-z.
[3] P. Sabatier, *Comptes Rendus* **1902**, *134*, 514.
[4] M. Bailera, P. Lisbona, L. M. Romeo, S. Espatolero, *Renewable Sustainable Energy Rev.* **2017**, *69*, 292–312, https://doi.org/10.1016/j.rser.2016.11.130.
[5] P. Tcvetkov, A. Cherepovitsyn, S. Fedoseev, *Sustainability* **2019**, *11*, 5834, https://doi.org/10.3390/su11205834.
[6] J. Baier, G. Schneider, A. Heel, *Front. Energy Res.* **2018**, *6*, 5, https://doi.org/10.3389/fenrg.2018.00005.
[7] M. Götz, J. Lefebvre, F. Mörs, A. McDaniel Koch, F. Graf, S. Bajohr, R. Reimert, T. Kolb, *Renew. Energy* **2016**, *85*, 1371.
[8] M. Specht, J. Brellochs, V. Frick, B. Stürmer, U. Zuberbühler, M. Sterner, G. Waldstein, *Erdoel Erdgas Kohle* **2010**, *126*, 342.
[9] T. Schaaf, J. Grünig, M. R. Schuster, T. Rothenfluh, A. Orth, *Energy, Sustain. Soc.* **2014**, *4*, https://doi.org/10.1186/s13705-014-0029-1.
[10] W. Li, H. Wang, X. Jiang, J. Zhu, Z. Liu, X. Guo, C. Song, *RSC Adv.* **2018**, *8*, 7651–7669, https://doi.org/10.1039/C7RA13546G.
[11] S. Ewald, M. Kolbeck, T. Kratky, M. Wolf, O. Hinrichsen, *Appl. Catal., A* **2019**, *570*, 376–386, https://doi.org/10.1016/j.apcata.2018.10.033.
[12] T. Burger, F. Koschany, O. Thomys, K. Köhler, O. Hinrichsen, *Appl. Catal., A* **2018**, *558*, 44–54, https://doi.org/10.1016/j.apcata.2018.03.021.
[13] C. H. Bartholomew, *Appl. Catal., A* **2001**, *212*, 17–60, https://doi.org/10.1016/S0926-860X(00)00843-7.
[14] W. L. Vrijburg, G. Garbarino, W. Chen, A. Parastaev, A. Longo, E. A. Pidko, E. J. M. Hensen, *J. Catal.* **2020**, *382*, 358–371, https://doi.org/10.1016/j.jcat.2019.12.026.
[15] M.-A. Serrer, K. F. Kalz, E. Saraçi, H. Lichtenberg, J.-D. Grunwaldt, *ChemCatChem* **2019**, *11*, 5018–5021, https://doi.org/10.1002/cctc.201901425.
[16] K. Zhao, Z. Li, L. Bian, *Front. Chem. Sci. Eng.* **2016**, *10*, 273–280, https://doi.org/10.1007/s11705-016-1563-5.
[17] K. Le, P. Jeong, *Catalysts* **2019**, 599, *9*, https://doi.org/10.3390/catal9070599.
[18] T. Burger, F. Koschany, A. Wenng, O. Thomys, K. Köhler, O. Hinrichsen, *Catal. Sci. Technol.* **2018**, *8*, 5920–5932, https://doi.org/10.1039/C8CY01834K.
[19] D. Qiang, T. Mei, Y. Liu, H. Jin, Z. Ye, Z. Li, S. Zhao, *Chem. Eng. J.* **2025**, *507*, 160839, https://doi.org/10.1016/j.cej.2025.160839.
[20] D. Qiang, T. Mei, Y. Liu, Z. Ye, Z. Li, S. Zhao, *Langmuir* **2025**, *41*, 14790–14799, https://doi.org/10.1021/acs.langmuir.5c00736.
[21] J. M. Polycarpo, M. Torquato, F. M. Z. Zotin, M. d. C. Rangel, A. C. Da Faro, L. A. Palacio, *Mol. Catal.* **2025**, *578*, 114965, https://doi.org/10.1016/j.mcat.2025.114965.
[22] X. Jia, X. Zhang, N. Rui, X. Hu, C.-J. Liu, *Appl. Catal., B* **2019**, *244*, 159–169, https://doi.org/10.1016/j.apcatb.2018.11.024.
[23] X. Xiao, J. Wang, J. Li, H. Dai, F. Jing, Y. Liu, W. Chu, *Int. J. Hydrogen Energy* **2021**, *46*, 33107–33119, https://doi.org/10.1016/j.ijhydene.2021.07.163.
[24] H. L. Huynh, Z. Yu, *Energy Tech.* **2020**, *8*, 1901475, https://doi.org/10.1002/ente.201901475.
[25] D. Weber, K. M. Wadlinger, M. M. Heinlein, T. Franken, *ChemCatChem* **2022**, *14*, e202200563, https://doi.org/10.1002/cctc.202200563.
[26] T. Franken, J. Terreni, A. Borgschulte, A. Heel, *J. Catal.* **2020**, *382*, 385–394, https://doi.org/10.1016/j.jcat.2019.12.045.
[27] S.-H. Lee, Y. J. Kwak, J.-W. Park, K.-T. Lee, *J. Korean Ceram. Soc.* **2023**, *60*, 536–546, https://doi.org/10.1007/s43207-022-00283-0.
[28] J. Thomas, N. Thomas, F. Girgsdies, M. Beherns, X. Huang, v. d. Sudheesh, V. Sebastian, *New J. Chem.* **2017**, *41*, 7356–7363, https://doi.org/10.1039/C7NJ00558J.
[29] Y. Jeong, I. Kim, J. Y. Kang, N. Yan, H. Jeong, J. K. Park, J. H. Park, J. C. Jung, *J. Mol. Catal. A: Chem.* **2016**, *168*:418–419.
[30] S. Abbas, H. Basma, J. Al Boukhari, *R. Awad, Appl. Phys. A* **2021**, 127, https://doi.org/10.1007/s00339-021-04669-5.
[31] Y. Kim, S. Kwon, Y. Song, K. Na, *J. CO2 Util.* **2020**, *36*, 145–152, https://doi.org/10.1016/j.jcou.2019.11.005.
[32] M. Pourbaix, *Atlas of electrochemical equilibria in aqueous solutions*, National Assoc. of Corrosion Engineers, Houston, TX **1974**.
[33] D. Weber, T. Engl, M. Raabe, A. Hutzler, M. Rubin, R. Dittmeyer, T. Franken, *Appl. Catal., A* **2025**, *708*, 120582, https://doi.org/10.1016/j.apcata.2025.120582.
[34] J. B. Goodenough, A. L. Loeb, *Phys. Rev.* **1955**, *98*, 391–408, https://doi.org/10.1103/PhysRev.98.391.
[35] S. Weber, R. T. Zimmermann, J. Bremer, K. L. Abel, D. Poppitz, N. Prinz, J. Ilsemann, S. Wendholt, Q. Yang, R. Pashminehazar, F. Monaco, P. Cloetens, X. Huang, C. Kübel, E. Kondratenko, M. Bauer, M. Bäumer, M. Zobel, R. Gläser, K. Sundmacher, T. L. Sheppard, *ChemCatChem* **2022**, *14*, e202101878, https://doi.org/10.1002/cctc.202101878.
[36] C. Li, Y.-W. Chen, *Thermochim. Acta* **1995**, *256*, 457–465, https://doi.org/10.1016/0040-6031(94)02177-P.
[37] Y. Du, J. Liu, X. Li, L. Liu, X. Wu, *Applied Organom. Chemis.* **2020**, *34*, https://doi.org/10.1002/aoc.5510.
[38] Q. Pan, J. Peng, T. Sun, S. Wang, S. Wang, *Catal. Commun.* **2014**, *45*, 74–78, https://doi.org/10.1016/j.catcom.2013.10.034.
[39] X. Guo, L.u Yao, X. Hou, X. Wu, Y. Zhang, Q. Zhu, Z. Guo, S. Li, Y. Jiang, S. Feng, K. Huang, *Chem. Sci.* **2022**, *13*, 9440–9449, https://doi.org/10.1039/D2SC02149H.
[40] T. S. Galhardo, A. H. Braga, B. H. Arpini, J. Szanyi, R. V. Gonçalves, B. F. Zornio, C. R. Miranda, L. M. Rossi, *J. Am. Chem. Soc.* **2021**, *143*, 4268–4280, https://doi.org/10.1021/jacs.0c12689.
[41] M. Langer, H. Freund, *Ind. Eng. Chem. Res.* **2024**, *63*, 10981–10996, https://doi.org/10.1021/acs.iecr.4c00819.
[42] S. Tada, M. Yokoyama, R. Kikuchi, T. Haneda, H. Kameyama, *J. Phys. Chem. C* **2013**, *117*, 14652–14658, https://doi.org/10.1021/jp404291k.

Manuscript received: August 29, 2025
Revised manuscript received: September 30, 2025
Accepted manuscript online: October 3, 2025
Version of record online: October 15, 2025